

## Full length article

# Modelling and characterisation of stress-induced carbide precipitation in bearing steels under rolling contact fatigue

H. Fu, E.I. Galindo-Nava, P.E.J. Rivera-Díaz-del-Castillo\*

SKF University Technology Centre, Department of Materials Science and Metallurgy, 27 Charles Babbage Road, University of Cambridge, CB3 0FS, UK

## ARTICLE INFO

## Article history:

Received 9 December 2016

Received in revised form

30 January 2017

Accepted 2 February 2017

Available online 4 February 2017

## Keywords:

Martensite

Rolling contact fatigue

Microstructural alteration

Lenticular carbides

Fatigue modelling

## ABSTRACT

The nucleation and growth of lenticular carbides (LCs) in bearing steels occur near to deformed ferrite bands after exposure to prolonged rolling contact fatigue (RCF). Since the first observations in 1947, a large number of attempts have been made to explain the formation mechanisms of such stress-induced microstructural alterations, but a reliable model was still not available. In this research, a novel theory is proposed to describe the carbon redistribution process during LC formation. The theory suggests a dislocation assisted LC growth mechanism on the basis of the classic Cottrell atmosphere formation theory. The mechanism considers (1)  $J_{LC} = J_d$ , the carbon flux equilibrium between LC thickening ( $J_{LC}$ ) and dislocation-assisted carbon migration ( $J_d$ ), and (2)  $M_0 = M_{LC} + M_b$ , the carbon mass conservation of the system, where  $M_0$  denotes the total amount of carbon within the system,  $M_{LC}$  denotes the amount of carbon within a LC, and  $M_b$  denotes the amount of carbon left within the ferrite band, respectively. The solution to these two equations, which addresses the problem that has been puzzling researchers for several decades, makes good predictions on LC thickening rate under various testing conditions. The stress-induced carbide precipitation was examined using high resolution characterisation techniques such as scanning and transmission electron microscopy, obtaining significant evidence to support the postulated theory. The successful description of LC growth implies a potential extension of the theory to other types of stress induced microstructural changes in bearing steels where carbon redistribution occurs. The model presented here provides a more comprehensive understanding of RCF from a microstructural point of view, and thus can enhance the accuracy of traditional bearing life prediction approaches.

© 2017 Acta Materialia Inc. Published by Elsevier Ltd. All rights reserved.

## 1. Introduction

Material instability of bearing steels under rolling contact fatigue (RCF) is manifested by the appearance of microstructural alterations, which alter the mechanical properties of the steel, diminish the capability of the material to sustain load, create favourable conditions for crack nucleation and propagation and lead to the final failure of the component [1,2]. One of the most striking alterations is the formation of plate-like lenticular carbides (LCs), adjacent to which are ferrite bands (Fig. 1 (b) and (c)). These microstructural features can be revealed by nital etchant, exhibiting white contrast to the surrounding matrix under visible light and usually being referred to as white etching bands (WEBs) [3–7]. Under normal RCF testing conditions, WEBs starts to appear at very

late stages of a bearing life, i.e.,  $> 10^8$  cycles, but it has been experimentally proved [8] that increasing either contact pressure or operational temperature can significantly accelerate the development of WEBs. Some authors [3,5,6] argued that prior to the nucleation of WEBs, the formation of a dark etching region (DER), another type of microstructural alteration resulting in martensite decay, is necessary, although experimental evidence shows that WEBs can occur in the absence of a DER when the parent martensite is softened by tempering to 670 HV [9]. The region where WEBs form, the subsurface of a bearing inner ring, has a strong correlation with the region of maximum shear stress as predicted by Hertzian theory [10], suggesting that the formation of WEBs is stress-induced, despite the fact that temperature also plays an important role [11]. Additionally, the special directionality of WEBs (shown in Fig. 1 (b)) is believed to be related to the local stress state [12,13].

A fully developed WEB can be 50–60  $\mu\text{m}$  in length and  $\sim 10 \mu\text{m}$  in width, while the thickness of a LC can reach 1  $\mu\text{m}$  [7]. The

\* Corresponding author.

E-mail address: [pejr2@cam.ac.uk](mailto:pejr2@cam.ac.uk) (P.E.J. Rivera-Díaz-del-Castillo).

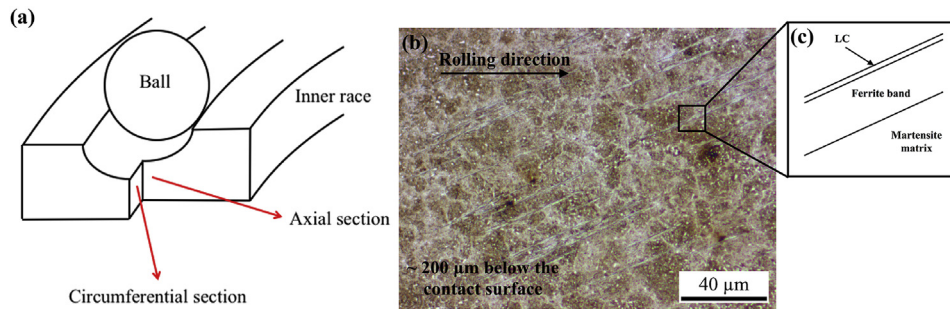


**Fig. 1.** (a) Circumferential and Axial sections of a bearing inner ring. (b) Optical microscopic image of the circumferential section of a bearing inner ring, where WEBs are formed at the subsurface with an inclination angle of  $\sim 30^\circ$  to the rolling direction. (c) Schematic showing the structure of a WEB consisting of a ferrite band and a LC adjacent to it.

presence of LCs is detrimental to the RCF resistance of the material as the interfaces between the LCs and the matrix were proved to be weak planes that may initiate damage when subjected to loading [4]. The ferrite bands, on the other hand, are produced by strain localization where carbide dissolution is found at their interiors [9,14]. Moreover, microindentation tests indicate material softening in the deformed ferrite [6,14], which is generally believed to be a consequence of carbon depletion by precipitating LCs at the boundaries [15]. With increasing number of cycles ( $N$ ), both LCs and ferrite bands thicken [7]. Therefore, the formation of WEBs can also be regarded as a process of carbon redistribution under RCF. However, it has been debated for decades as to the driving force for such carbon migration. The early theories [4,9,16] suggesting the microstructural changes result from tempering due to local temperature rise at the subsurface have no evidence to support. Moreover, the finding of the threshold stresses under which no microstructural change occurs, no matter how long the bearing operation time is, supports a stress-induced mechanism [5]. Bush et al. [5] referred to the fatigue of aluminium alloys and postulated a material extrusion-intrusion theory, where the importance of spherical carbide shearing is emphasized, to explain the origination of LCs. Besides, Swahn et al. [3] argued the energy increase caused by plastic deformation is the driving force for carbon flowing towards the surrounding matrix. Buchwald and Heckel [7] presumed the outflow of carbon from ferrite bands to LCs results from both carbon concentration and stress gradients, and for the first time put forward a quantitative model to calculate the thickening rate of LCs based on this theory. However, the results demand a temperature rise of at least 200 °C to achieve the observed growth rate, which is unrealistic. After that, Polonsky and Keer [13] argued that carbon injection into the solid solution during dislocation annihilation promotes the carbon leaving ferrite bands and postulated a diffusion-based mechanism, yielding better predictions on Buchwald and Heckel's data [7]. Nonetheless, Polonsky and Keer's model is rather approximated and the effect of applied stress was not taken into consideration despite the experimental evidence that increasing contact pressure accelerates WEB formation [8]. In this context, focus should shift to the rearrangement of dislocations in ferrite bands, although this was previously seldom considered to be related to the redistribution of carbon. This is because: (i) the ferrite bands stem from plastic deformation and may contain a high number density of dislocations; (ii) the strain fields around dislocations can attract carbon atoms as pointed out by Cottrell and Bilby [17], and thus result in a strong interaction between carbon in solid solution and dislocations; (iii) the cyclic loading of bearing operation generates a large amount of dislocation gliding, which can be the source of the driving force for carbon migration. Briefly speaking, the most likely mechanism for LC formation is that the gliding dislocations

act as vehicles transporting carbon atoms to the band-matrix boundaries and precipitate LCs. Therefore, in this work, a dislocation-assisted carbon migration process is postulated to predict LC growth. The model is compared with experimental observations under various conditions. In addition, high resolution characterisation was carried out on WEBs to investigate the redistribution of carbon.

## 2. LC thickening model

### 2.1. Dislocation assisted carbon migration theory

When subjected to cyclic loading, a bearing inner ring experiences stress pulses with a period of  $t_c$  when the balls roll over. Such stress history is schematically illustrated in Fig. 2. Within each stress pulse, if the local stress exceeds the threshold for dislocation movement, the dislocations will be pulled away from their original carbon atmospheres, glide a distance and then come to a stop until the advent of the next stress pulse after  $t_c$ . Therefore, dislocation glide in each stress cycle is discontinuous, and  $t_c$  is the time interval for carbon in the surrounding matrix to return back to a dislocation that just moved, forming again a Cottrell atmosphere around it. According to Cottrell and Bilby [17], the total number of carbon atoms ( $n_C$ ) that can be captured by a free dislocation per unit length can be expressed as:

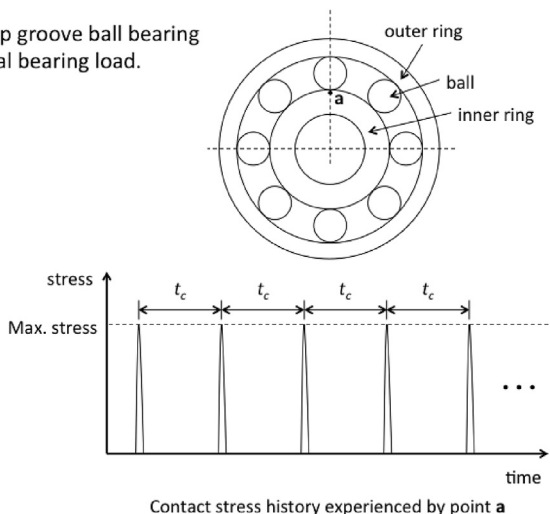


**Fig. 2.** Schematic of a 6309 type bearing geometry and the loading history experienced by a subsurface point during bearing operation.  $t_c$  is the time interval between each stress cycle.

$$n_c = 3 \left( \frac{\pi}{2} \right)^{\frac{1}{3}} \left( \frac{ADt_c}{kT} \right)^{\frac{2}{3}} C_{Vb}, \quad (1)$$

where  $A$  is the interaction energy between a carbon atom and the dislocation strain field which can be obtained from Ref. [17],  $D$  is the diffusion coefficient of carbon atoms in  $\alpha$  iron,  $k$  is the Boltzmann constant,  $T$  is temperature and  $C_{Vb}$  is the carbon concentration in the surrounding matrix, in this case the carbon concentration within the ferrite bands. For a bearing operating at a rotational speed  $\dot{N}$ ,  $t_c$  can be calculated as  $t_c = \frac{1}{\dot{N}}$ . At the early stage of RCF, a plastic shakedown phase can be achieved in the material, where a steady plastic flow occurs thereafter [18]. Then the repetitive segregation-desegregation of carbon atoms to gliding dislocations creates a carbon flux along with the dislocation flow. In this respect,  $n_c$  actually describes the capability of dislocations to transport carbon atoms. Considering a system with mobile dislocation density  $\rho_m$  and average gliding distance  $\Delta L$  within each stress cycle, the carbon flux ( $J_d$ ) resulting from dislocation flow can be expressed as:

$$J_d = \rho_m \Delta L \dot{N} n_c. \quad (2)$$

Note the term  $\Delta L \dot{N}$  represents the equivalent dislocation speed under RCF. According to the Orowan equation, plastic strain is manifested by the gliding of mobile dislocations, and in the case of rolling contact, the plastic strain per stress cycle ( $\Delta\gamma$ ) can hence be described as:

$$\Delta\gamma = b \rho_m \Delta L, \quad (3)$$

where  $b$  denotes the magnitude of the Burgers vector. Combining equations (1)–(3), the carbon flux thus becomes:

$$J_d = \frac{\Delta\gamma \dot{N}}{b} \left[ 3 \left( \frac{\pi}{2} \right)^{\frac{1}{3}} \left( \frac{AD}{kT\dot{N}} \right)^{\frac{2}{3}} C_{Vb} \right]. \quad (4)$$

This mechanism is referred to as dislocation-assisted carbon migration. Except for some testing conditions such as temperature and rotational speed that directly control the magnitude of  $J_d$ , contact pressure ( $p_0$ ) controls  $J_d$  indirectly via  $\Delta\gamma$ , the value of which can only be obtained experimentally from other simpler fatigue tests.

## 2.2. LC precipitation

The proposed dislocation-assisted carbon migration mechanism is applied to the growth of LCs. Prior to the precipitation of LCs, ferrite bands are formed under cyclic subsurface shearing. The shear stress can be so severe that the parent martensite loses the initial plate-like microstructure and decays into a type of deformed ferrite, during which process a large amount of mobile dislocations are created and forced to glide to undertake plastic deformation. Martensite itself can be regarded as a carbon-supersaturated ferrite phase which tends to remove carbon from the solid solution to form carbides, due to the solubility of carbon in ferrite phase being very low ( $< 0.02$  wt%) at the bearing operation temperature [1]. The dislocation gliding along with a high level of local hydrostatic compression stress causes the dissolution of both globular and tempered carbides [7], which adds to the supersaturation of carbon in the ferrite bands. Therefore, the formation of precipitates is thermodynamically favourable, but the operation temperature of rolling contact fatigue tests (usually  $< 100$  °C) is too low to cause noticeable thermal diffusion of carbon such that the kinetics of carbide formation is suppressed. In the case of LCs, however, the carbon flux caused by gliding dislocations from the carbon-

supersaturated ferrite band towards the ferrite band boundaries contributes to such kinetics. This is the reason why LCs are only observed along deformed ferrite bands where massive dislocation gliding occurs. Fig. 3 (a) illustrates the three formation stages of a LC. At stage I, as pointed out by some authors [3,6], the boundary between a ferrite band and the matrix becomes favourable for carbide nucleation, and therefore numerous carbide nuclei are formed first along the ferrite band boundary. With further carbon transportation towards the ferrite boundary, these nuclei grow into carbide crystallites, which then coalesce into a long and thin LC at stage II. At stage III, the carbide crystallites continue growing towards the interior of the ferrite band, leading to thickening of the LC at the microstructural level. It should be noted that the proposed LC formation mechanism is different from diffusion-controlled carbide precipitation during heat treatment of the steel, as the lenticular morphology of LCs results from the coalescence of numerous carbide crystallites which nucleate immediately once a deformed band is formed, rather than through continuous lengthening along ferrite band boundaries. In a word, the length of a LC is dependent upon the length of the ferrite band, while its thickness of gradually increases until all the carbon in the ferrite band is consumed. The proposed mechanism is validated by TEM as discussed in Section 4.2.

With the dislocation transported carbon contributing to the proceeding LC front, there exists an equilibrium between the carbon flux of LC thickening ( $J_{LC}$ ) and  $J_d$  at the LC-ferrite interface, namely,  $J_{LC} = J_d$ . Fig. 3 (b) illustrates the dislocation assisted carbon migration mechanism occurs in ferrite bands. Therefore, the equilibrium is further expressed as:

$$\frac{dI_{LC}}{dt} (C_{V\theta} - C_{Vb}) = \frac{\Delta\gamma \dot{N}}{b} \left[ 3 \left( \frac{\pi}{2} \right)^{\frac{1}{3}} \left( \frac{AD}{kT\dot{N}} \right)^{\frac{2}{3}} C_{Vb} \right], \quad (5)$$

where  $I_{LC}$  denotes the thickness of the LC,  $t$  denotes the operation time which can be converted to the number of cycles via  $N = t\dot{N}$ ,  $C_{V\theta}$  denotes the carbon concentration within LCs by assuming the same crystal structure as the most ordinary  $\theta$ -type carbides, and  $C_{Vb}$  denotes the carbon concentration of the ferrite bands. Equation (5) reveals the kinetics of LC formation. Meanwhile, at any point during this process, the amount of carbon within the system equals the sum of that within the LC and the ferrite band, namely,  $M_0 = M_{LC} + M_b$ , where  $M_0$  denotes the total amount of carbon within the system,  $M_{LC}$  denotes the amount of carbon within a LC, and  $M_b$  denotes the amount of carbon left within the ferrite band, respectively, which leads to the following equation:

$$\lambda C_{V0} = I_{LC} C_{V\theta} + (\lambda - I_{LC}) C_{Vb}, \quad (6)$$

where  $C_{V0}$  is the initial carbon concentration of the system, which is equal to the carbon concentration of the alloy due to complete carbide dissolution in ferrite bands, and  $\lambda$  is the width of a fully developed WEB, which was estimated to be  $\sim 9 \mu\text{m}$  [7,13]. Equation (6) gives the evolution of  $C_{Vb}$  as follows:

$$C_{Vb} = \frac{\lambda C_{V0} - I_{LC} C_{V\theta}}{\lambda - I_{LC}}. \quad (7)$$

By substituting Equation (7) into Equation (5) and solving the differential equation, a LC thickening process can be obtained.

## 3. Experimental validation

### 3.1. RCF tests

The experimental data of  $I_{LC}$  evolution with respect to  $N$  were

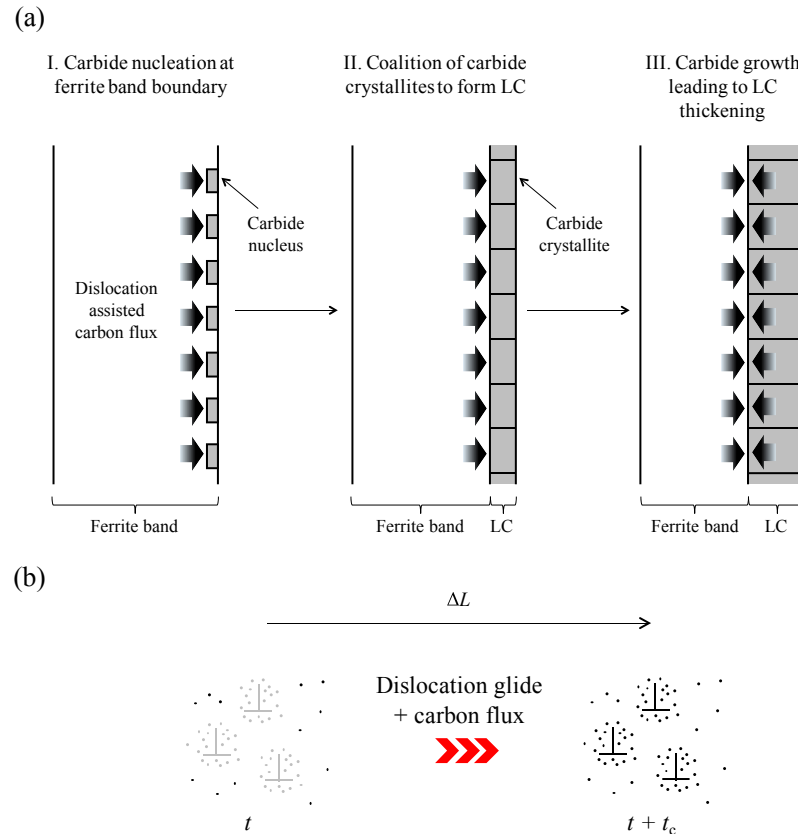


**Fig. 3.** Schematic of LC growth as a result of dislocation assisted carbon migration mechanism. (a) LC formation along a ferrite band with three stages. (b) Cottrell atmospheres dragged by gliding dislocations within one stress cycle.

obtained from both Buchwald and Heckel's work [7] (Exp 1) and this research (Exp 2). The material for the RCF samples used in this research is 100Cr6 bearing steel with the composition listed in Table 1. The material was quenched in a salt bath from the austenitization temperature of 860 °C, followed by tempering at 220 °C for 240 min for carbide precipitation and residual stress release. The resultant microstructure contains spherical cementite particles (~ 4 vol%) and nano-sized tempered carbides (~ 10 vol%) distributed in a matrix of martensite. No retained austenite is present. The hardness of the material is ~ 720 HV30.

Three through hardened deep groove ball bearings of 6309 type were tested on a SKF R2 test rig [19] for predetermined numbers of cycles to reproduce WEBs at different formation stages. The RCF tests were carried out by applying a radial load to the balls, resulting in a contact pressure of 3.3 GPa. The rotational speed was controlled to be 6000 rpm (note there are about 5 cycles within 1 revolution for 6309 bearings), and the outer ring temperature was measured to be 70 °C. The tests were suspended at  $5 \times 10^8$ ,  $10^9$  and  $2 \times 10^9$  cycles, respectively. Note the material used in this research is identical to that used in Exp 1.

After the RCF tests, the fatigued bearing inner rings were cut through the middle of the tracks to show their circumferential sections (Fig. 1 (a)), followed by careful surface preparation and nital etching for microscopic investigation. The statistical analysis

of the LCs was conducted under a scanning electron microscope (SEM), and the thickness of at least 50 LCs from the most populated region were measured and averaged for each sample. The measurement results are shown in Table 2, where a significant thickening trend of LCs with increasing number of cycles can be seen.

### 3.2. Modelling results and discussion

Due to the complex stress state under rolling contact,  $\Delta\gamma$ , a key input for modelling, cannot be directly measured from RCF tests. Therefore, uni-axial repetitive push tests were performed with various stress ranges on cylindrical samples made of the same material, in order to estimate  $\Delta\gamma$  under RCF. By fitting to the experimental data, a relationship between  $\Delta\gamma$  and the equivalent shear stress ( $\tau_{max}$ ) can be obtained:  $\Delta\gamma = 4.757 \times 10^{-5} \tau_{max} + 1.72 \times 10^{-5}$ , where  $\tau_{max}$  is in GPa. Note this equation is valid only in the plastic regime. The detailed testing method and data analysis can be found in Appendix A.

By inputting the given testing conditions and material parameters, the proposed mechanism described by Equations (5) and (6) can be solved, yielding the evolution of  $l_{LC}$  and  $C_{Vb}$  with respect to  $N$ . The modelling results in comparison with the experimental data on LC thickening are shown in Fig. 4 (a). For both cases, the

**Table 1**  
Composition of 100Cr6 bearing steel (wt%).

C	Cr	Mn	Si	Cu	Ni	Mo	Al
0.97	1.38	0.28	0.28	0.21	0.18	0.06	0.04

**Table 2**  
LC thickness evolution with increasing number of cycles.

N/cycles	$5 \times 10^8$	$10^9$	$2 \times 10^9$
$l_{LC}/\mu\text{m}$	$0.12 \pm 0.04$	$0.24 \pm 0.07$	$0.43 \pm 0.06$

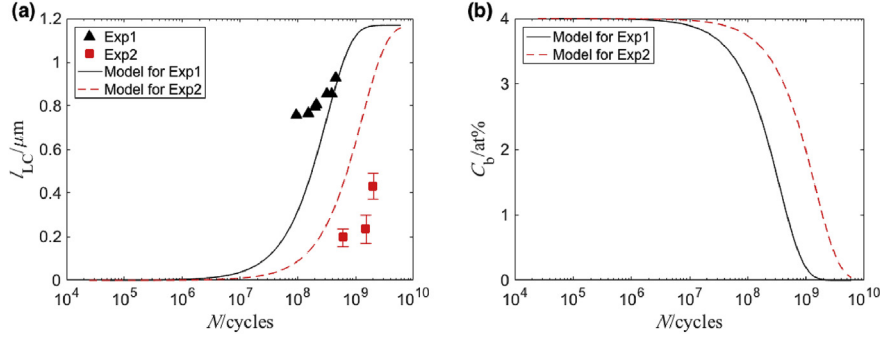


**Fig. 4.** Modelling results for Exp 1 and 2. (a) Evolution of LC thickness with number of cycles and (b) carbon depletion with number of cycles.

observed LC thickening rates are well predicted, suggesting the accuracy of the proposed mechanism and model. Besides, Fig. 4 (b) shows the corresponding carbon depletion in ferrite bands during LC thickening, which explains the material softening in WEBs. Moreover, with the same material and contact pressure, LC thickening is faster in Exp 1 than in Exp 2 because of higher operation temperature ( $105^\circ\text{C}$  vs.  $70^\circ\text{C}$ ), despite the deceleration effect from higher rotational speed (9700 rpm vs. 6000 rpm).

The model is also applied to RCF tests from the literature which only report the number of cycles where WEBs were first observed. In order to compare the calculation results with the experimental observation, a new term WEB%, defined as  $\text{WEB\%} = \frac{C_{v0} - C_{vb}}{C_{v0}} \times 100$ , is introduced to account for the extent of WEB formation. According to the definition, WEB development is quantified via the extent of carbon depletion within ferrite bands, and when all the carbon is transported to LCs, the formation of WEBs is 100% complete. Note that most of these RCF tests were carried out on 100Cr6 steel with an alternative tempering treatment:  $160^\circ\text{C}$  for 90–120 min, which results in different material response to the applied load and consequently alters  $\Delta\gamma$ . Hence a new equation, being  $\Delta\gamma = 5.9 \times 10^{-5} \left( \frac{\tau_{\max}}{0.4} - 1 \right)^3$  where  $\tau_{\max}$  is in GPa, is obtained by referring to the push-pull tests carried out on such material by Christ et al. [20]. The fitting of the experimental data is shown in Fig. 5 (a). As for the RCF tests, 3 sets of data under various testing conditions were selected from the literature for comparison: Exp 3 [3] ( $p_0 = 3.2 \text{ GPa}$ ,  $T = 50^\circ\text{C}$ ,  $\dot{N} = 6000 \text{ rpm}$ ,  $N$  (WEBs appearance) =  $2 \times 10^8$  cycles); Exp 4 [3] ( $p_0 = 3.7 \text{ GPa}$ ,  $T = 50^\circ\text{C}$ ,  $\dot{N} = 6000 \text{ rpm}$ ,  $N$  (WEBs appearance) =  $5 \times 10^8$  cycles); and Exp 5 [5] ( $p_0 = 3.2 \text{ GPa}$ ,  $T = 30^\circ\text{C}$ ,  $\dot{N} = 2200 \text{ rpm}$ ,  $N$  (WEBs appearance) =  $1.2 \times 10^9$  cycles). The modelling results for each case are presented in Fig. 5 (b), and vertical lines are drawn at the

reported  $N$  values where WEBs were first observed. The highlighted intersection points between the calculated curves and the vertical lines all lie in the early stages of WEB formation (20%–30%), which, according to the model, should result in LCs of the thickness 0.3–0.4  $\mu\text{m}$ . This magnitude is roughly the resolution limit of optical microscopy. Moreover, the trends of the curve shift agree with the experimental observation.

The testing conditions that control the formation rate of LCs are contact pressure, operation temperature and rotational speed. Higher operation temperature enhances carbon diffusion in the matrix, and thus enables more carbon to be captured by dislocations, accelerating LC thickening (Fig. 6 (a)). Higher contact pressure, on the other hand, results in higher maximum shear stress at the subsurface and consequently, higher plastic shear strain amplitude. According to the proposed mechanism for carbon migration, dislocations act as vehicles transporting carbon in the solid solution during dislocation glide, so severer plastic deformation, undertaken by higher mobile dislocation density and/or longer mean glide distance, definitely promotes this type of dislocation flow and the corresponding carbon flux (Fig. 6 (b)). Increasing rotational speed, however, has a negative effect on carbon migration as higher rotational speed decreases the time interval for carbon segregation to dislocations in each stress cycle, which reduces the amount of carbon in the carbon flux (Fig. 6 (c)). The acceleration effect of operation temperature and deceleration effect of rational speed on WEB formation agrees with the argument by Polonsky and Keer [13]. Nevertheless, the predictions made by the present model are more accurate than any previous models. Fig. 4 (a) demonstrates the model is capable of predicting the trend of LC formation under various testing conditions, which is crucial to industry and thus reduce the necessity of carrying out a large number of time consuming RCF tests, while Fig. 5 (b)

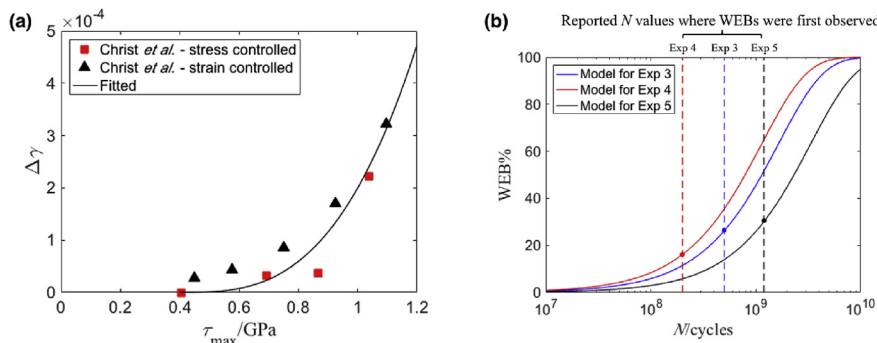


**Fig. 5.** Modelling results for Exp 3, 4 and 5. (a) Fitted  $\Delta\gamma$ - $\tau_{\max}$  relationship from push-pull tests by Christ et al. [20] and (b) calculated WEB formation curves comparing with the  $N$  values for WEB appearance.

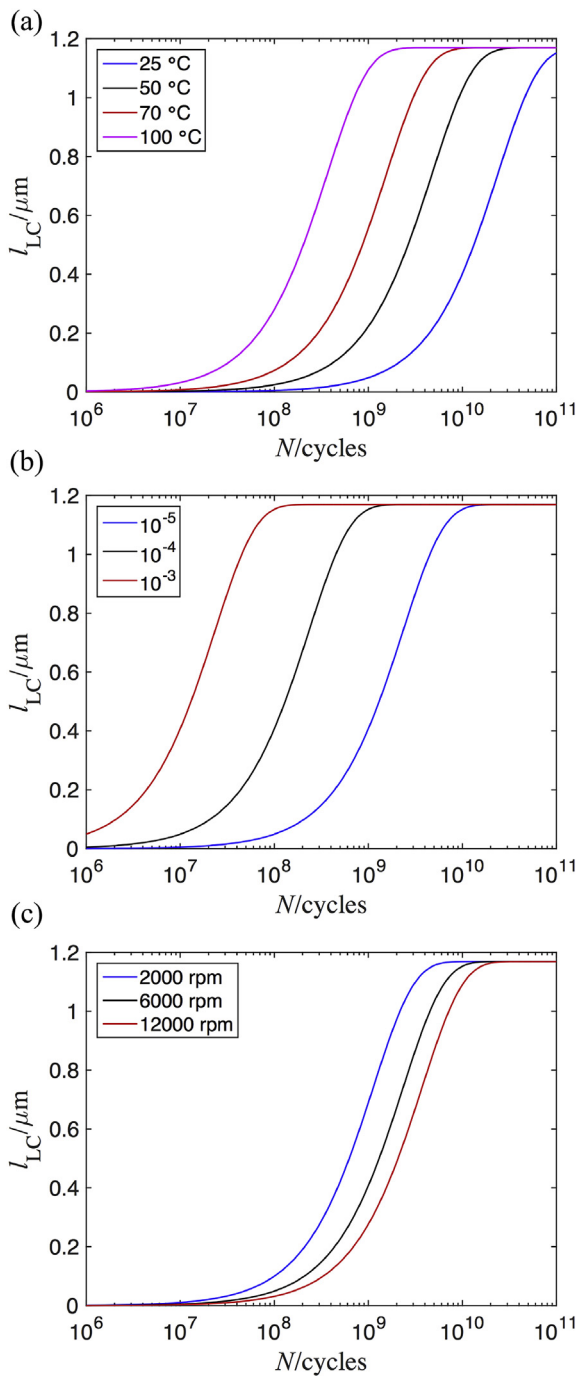


**Fig. 6.** Effects of RCF testing conditions on LC thickening. (a) Thickening curves under increasing  $T$  with other conditions constant ( $\Delta\gamma = 6 \times 10^{-5}$ ,  $\dot{R} = 6000$  rpm); (b) thickening curves under increasing  $\Delta\gamma$  with other conditions constant ( $T = 100^\circ C$ ,  $\dot{R} = 6000$  rpm); (c) thickening curves under increasing  $\dot{R}$  with other conditions constant ( $T = 100^\circ C$ ,  $\Delta\gamma = 6 \times 10^{-5}$ ).

demonstrates the model can be applied to different types of steels.

#### 4. Microscopic investigation

##### 4.1. SEM

SEM investigation was carried out under an FEI Nova NanoSEM 450 SEM, and energy-dispersive X-ray spectroscopic (EDS) mapping was also performed on a WEB. The characterisation results

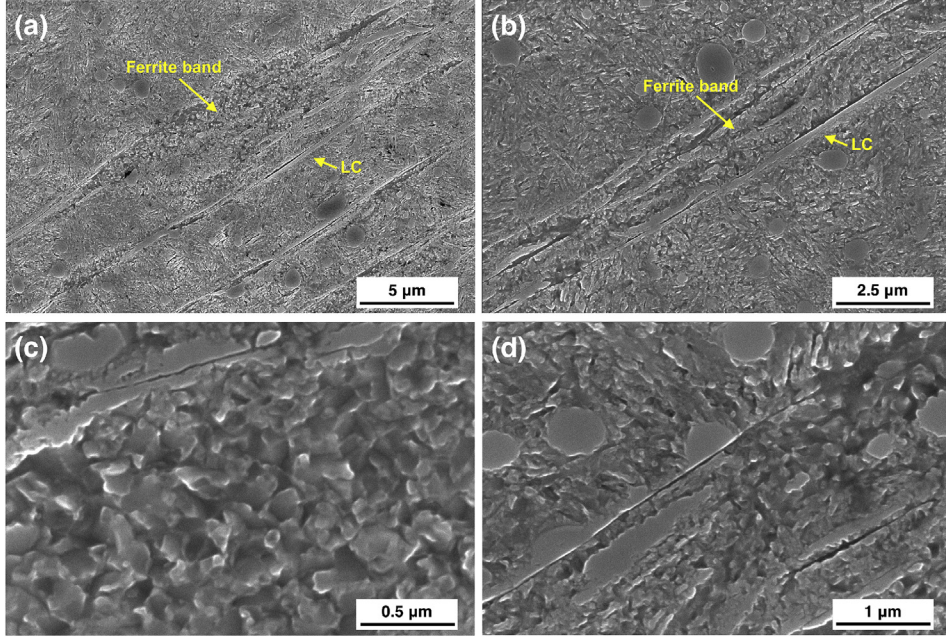
reveal that a WEB consists of a ferrite band with LCs adjacent to it (Fig. 7 (a) and (b)). LCs can appear on either or both sides of a ferrite band, but the former case is more often observed. A very fine microstructure is found within the deformed ferrite bands compared with the surrounding matrix, as shown in Fig. 7 (c). In addition, Fig. 7 (d) illustrates when a developing WEB is encountered with pre-existing  $M_3C$  particles, the latter can be dissolved. Similar phenomena have also been observed by other authors [21].

Fig. 8 (c) – (e) presents the results of chemical mapping obtained from EDS. A WEB consisting of a LC and a ferrite band can be seen from the SEM image in Fig. 8 (a). The size of the LC is much larger than the spherical  $M_3C$  particles. Comparing the distributions of Fe in Fig. 8 (c) and C in Fig. 8 (e), it is obvious that C is enriched in the LC and the  $M_3C$  particles while the concentration of iron is lower in these regions. Moreover, in Fig. 8 (e), carbon depletion is found in the ferrite band (region "A") adjacent to the LC, compared with the uniformly spread C in the surrounding matrix (region "B"). This indicates that C is segregated from the ferrite band to the LC during WEB formation. Fig. 8 (d) shows Cr is strongly segregated to the  $M_3C$  particles but not to the LC. Cr enrichment in the  $M_3C$  particles can be expected as these particles are formed at the spheroidisation stage [1] and the diffusion of Cr during the subsequent RCF test is negligible given such low diffusion coefficient of Cr at the bearing operation temperature. Carbon, on the other hand, can be transported by gliding dislocations towards LCs. Besides, the fact that Cr enrichment is not found in the LC rules out the argument that LCs originate from the deformation of the pre-existing chromium-enriched carbide particles [5], and hence LCs are in nature iron carbides.

#### 4.2. FIB/TEM

A TEM lamella was prepared from the severest fatigued sample ( $2 \times 10^9$  cycles) using FIB in a FEI Helios NanoLab workstation. The milled lamella contains a cross section along the width of a WEB. TEM observations were carried out in a FEI Oris TEM/STEM 80-200 TEM where electron energy loss spectroscopy (EELS) was also performed to quantify the carbon content of the LCs.

Fig. 9 (a) is a TEM image of the FIB lamella. A part of the Pt protection was removed during final milling, indicating that the sample thickness had reached the lower limit. But due to the wedge-shape nature of the lamella, the optimum electron transparency is always the region near the Pt protection. From Fig. 9 (a), the cross section of a WEB can be seen in the middle of the lamella, with a ferrite band in between two LCs. An obvious cellular microstructure can be found inside the ferrite band, which is an indication of plastic deformation and consequent dislocation rearrangement. It should also be noted that spherical  $M_3C$  particles can be found in the matrix but absent in the WEB. Fig. 9 (b) presents the boundary of the WEB at higher magnification and a LC lies in between the ferrite band and the matrix. The LC exhibits a columnar structure with units of about 100 nm in width. A more detailed microstructure image of the LC is shown in Fig. 10. A similar microstructure was also observed by Lund et al. [9] and was described as "rung-like carbide disks". Since the LCs are reprecipitated, one plausible explanation to this specific microstructure, in agreement with the analysis by Swahn et al. [3], is that each small columnar unit follows the nucleation of a carbide crystallite, and when carbon is transported to the boundary to participate into further growth of the crystallites, they grow towards the inner part of the ferrite band at a constant pace. Therefore, the interfaces between the columns are actually grain boundaries. The fact that these grain boundaries are parallel to each other and perpendicular to the WEB boundary is a strong indication of carbon flux in the



**Fig. 7.** SEM images of WEBs from the circumferential section of the sample run for  $2 \times 10^9$  cycles. (a) A bunch of WEBs found at the subsurface; (b) A WEB consisting of a deformed ferrite band and LCs; (c) very fine microstructure within a deformed ferrite band; (d) M<sub>3</sub>C particles dissolved by a WEB.

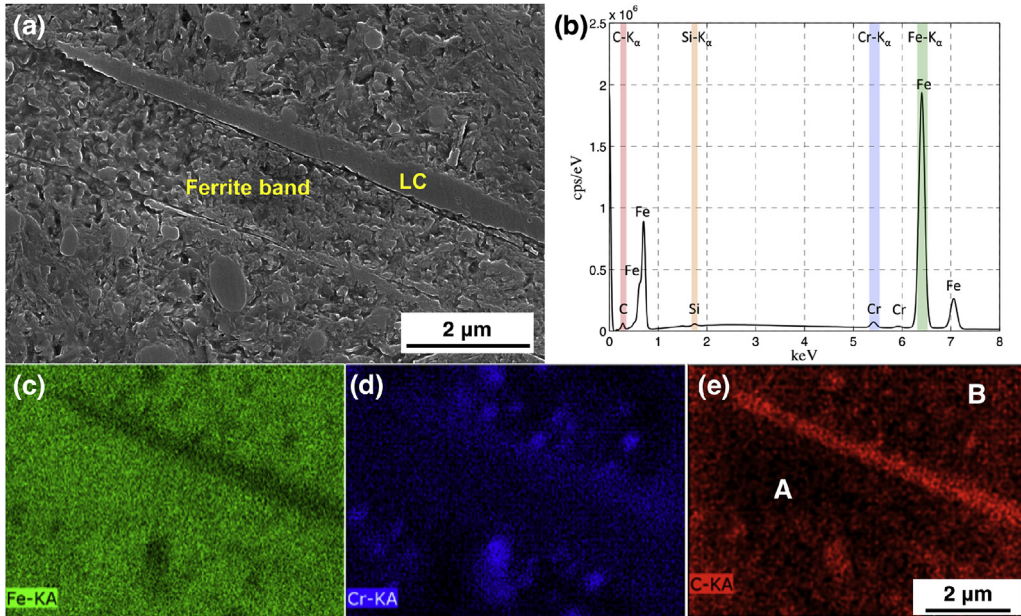


**Fig. 8.** Results of EDS chemical mapping on a WEB. (a) SE image of the EDS area containing a WEB; (b) spectrum of the EDS test showing the detected elements from the area. The K<sub>α</sub> peaks of each element are also marked; (c)–(e) chemical mapping results of Fe, Cr and C, respectively.

direction of crystallite growth, which is most likely to be perpendicular to the WEB boundary. The observed LC morphology and growth direction is strong evidence for the proposed LC formation mechanism illustrated in Fig. 3 (a). Nevertheless, LCs can be lengthened with increasing number of cycles, where new carbide nuclei are formed along with the lengthening of ferrite bands. However, this involves a complex local stress state and material plasticity that requires further investigation. For the time being, the proposed model considers a simplified scenario only, which could be the reason why the measured average LC thickness is sometimes

lower than the predictions.

The ferrite band, as shown in Fig. 9 (b), contains finely distributed equiaxed dislocation cells, in agreement with the descriptions from the literature, and the sizes of the cells are in the range of 100–200 nm. Note that dislocation cells can also be found in the matrix near the LC. The formation of dislocation cells in martensite under RCF is a result of local plastic deformation, but what is observed in WEBs is different from that in white etching areas (WEAs) – another type of microstructural alteration under RCF that also exhibits similar martensite decay with dislocation cell

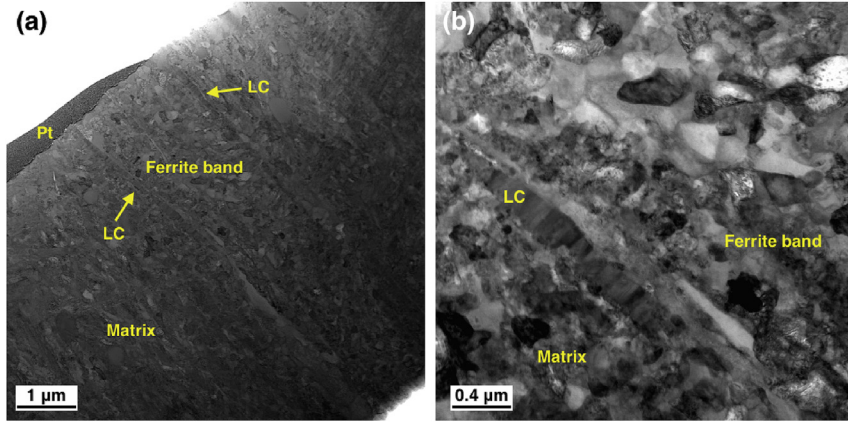


**Fig. 9.** TEM characterization on a WEB. (a) TEM lemella prepared by FIB; (b) TEM image showing a LC lying between the ferrite band and the matrix.

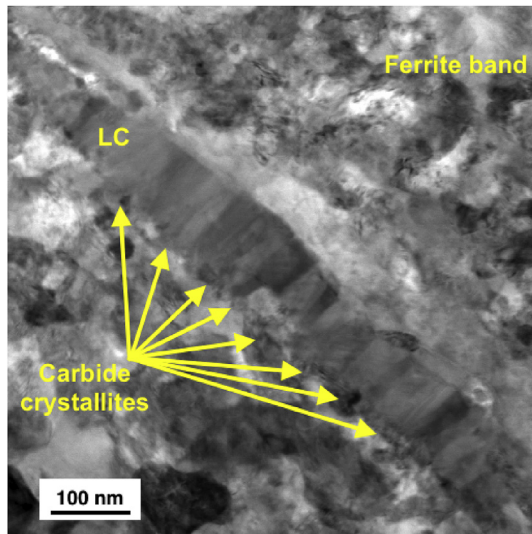


**Fig. 10.** High magnification image showing the unique microstructure of a LC. The long and thin LC consists of small carbide blocks, which are carbide crystallites with clear grain boundaries between each other.

formation, carbide dissolution and white contrast under visible light after etching with nital [22]. WEAs are always accompanied by cracks initiated from foreign inclusions and form in a butterfly wing shape. Extensive characterisation and analysis on WEAs [23–26] has led to the conclusion that WEAs stem from the repetitive beating and rubbing of the crack surfaces and the corresponding microstructural change is of the same nature as that induced by severe plastic deformation (SPD). Additionally, the stress concentration around inclusions plays an important role in the formation of WEAs [27,28]. In the case of WEBs, however, microstructural changes occur in absence of any cracks or observable stress concentrators, and the dislocation substructure is coarser than the ferrite grains in WEAs (100–200 nm vs. 10–50 nm). Besides, WEBs appear much later than WEAs under the same testing conditions (10<sup>4</sup> cycles vs. 10<sup>8</sup> cycles). More importantly, in spite of carbide dissolution in both cases, the dissolved carbon in WEAs is found segregated to dislocation cell walls [29] which leads to a distinct increase in hardness, whereas the dissolved carbon in WEBs is transported across the length of a few microns and re-precipitated as LCs along the boundaries leaving a softer ferrite band. Therefore, the formation of WEBs is more likely to be gradual matrix degradation accompanied by carbon redistribution rather than the drastic microstructural transition caused by SPD.

In order to determine the carbon concentration in LCs, EELS was carried out. As shown in Fig. 11 (a), a region containing a LC in the middle was selected for subsequent mapping for carbon. A

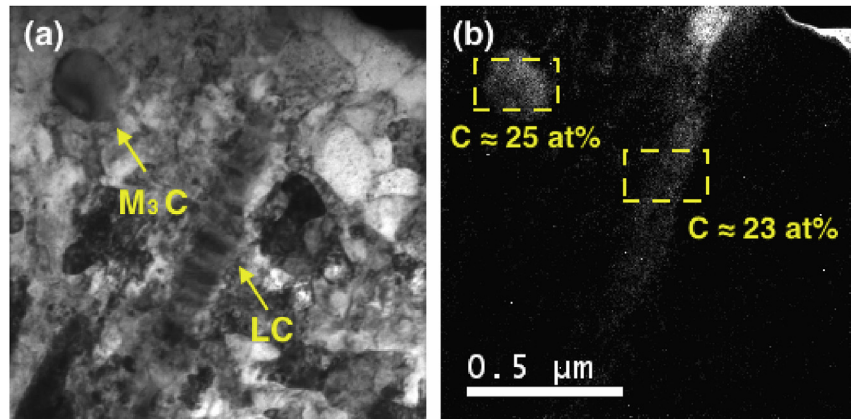


**Fig. 11.** EELS result on the LC. (a) Energy filtered TEM image of the LC with a M<sub>3</sub>C particle for reference; (b) C map obtained from the EELS test. The dash-line rectangles mark where quantitative analysis was carried out. The two images are of the same magnification and share the same scale bar.

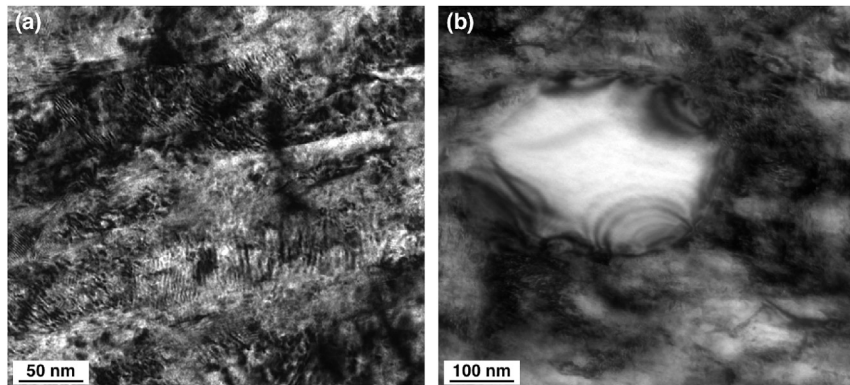


**Fig. 12.** TEM characterization on the matrix surrounding the WEB. (a) Martensitic matrix containing finely distributed nano-sized carbides; (b) An M<sub>3</sub>C particle with dislocation loops inside, indicating the plastic deformation in the matrix.

spherical carbide particle with known composition (M<sub>3</sub>C, M = Fe or Cr) was also included for reference. After careful processing of the spectrum, a carbon map was obtained, as presented in Fig. 11 (b). Carbon enrichment can be clearly seen in both the M<sub>3</sub>C particle and the LC, which agrees with the finding from EDS. The quantitative analysis performed in the areas marked the dash-line rectangles yields a carbon content in the LC of about 23 at%, very close to the expected 25 at% in M<sub>3</sub>C. Hence LC crystal structure is expected to be cementite. This result is consistent with the key assumption of the proposed model.

The microstructure of the matrix surrounding the WEB was also studied. As shown in Fig. 12 (a), some needle-like precipitates are found in the matrix, with their elongation directions roughly perpendicular to the elongation direction of a large martensite plate. This agrees with the microstructural description of tempered martensite [30], but there also exists a large number of much finer carbide fragments, suggesting the onset of precipitate dissolution before WEB nucleation. The plastic deformation in the matrix can be visualised by looking at a spherical M<sub>3</sub>C particle, as shown in Fig. 12 (b), where dislocation loops are generated from the sources at the particle-matrix interface and propagate into the particle.

## 5. Conclusions

A novel theory has been postulated to explain stress-induced LC formation in bearing steels under RCF. The growth of LCs consumes the carbon within adjacent ferrite bands and thus WEBs are formed. The special stress history of cyclic rolling contact triggers a dislocation assisted carbon migration mechanism, with the magnitude of carbon flux dependent upon the operation conditions of RCF tests. The LC thickening process with increasing number of cycles is described by two key equations, the carbon flux equilibrium at the LC-ferrite interface and carbon mass conservation. The calculated LC thickening rates were compared with the experimental results and good agreement was achieved. It has been demonstrated that the model can accurately predict LC thickening (WEB formation) under various RCF testing conditions and material types.

High resolution characterisation was carried out on WEBs. SEM imaging reveals the structure of WEBs, with distinct features compared to the parent martensite; also, pre-existing spherical cementite particles can be dissolved by developing WEBs, rather than being deformed; EDX mapping effectively visualizes the elemental distribution within a WEB, and confirms the carbon

migration towards LCs; FIB/TEM shows the cellular structure within the deformed ferrite bands, which is evidence for dislocation glide. Higher magnification TEM shows unique morphology of LCs consisting of carbide crystallites with the growth direction of LCs in agreement with the proposed mechanism. EELS confirms LCs to be  $\theta$ -type carbides.

The formation of WEBs is a detrimental microstructural transition during bearing fatigue controlled by the migration of carbon. The proposed model can be potentially extended to other stress-induced microstructural decay which involves element redistribution. Future work is suggested to study the relationship between such microstructural features and bearing life.

## Acknowledgements

This work was financed by SKF Engineering & Research Centre. The authors are grateful to Dr J. Lai for the fruitful discussions. The authors would also like to express gratitudes to Mr M.A. Stopher for assistance on TEM operation.

## Appendix A. Cyclic compression tests

The cyclic compression tests were conducted on a Mayes 100 KN LCF mechanical tester to estimate the plastic strain amplitude during RCF. The specimens used are cylinders of 3 mm diameter and 5 mm length. The set-up of the tests is shown in Fig. A1 (a), where the cylinder was placed between two blocks made of the same material as the compression sample. A 1 mm KFG-1N-120-C1-11 strain gage produced by KYOWA was glued to the side of the sample. Repetitive compressive load was delivered by the upper head of the tester while the lower stage remained stationary. The load was applied at 15 Hz following a sinusoid pattern with a constant maximum load magnitude in each stress cycle controlled by computer programme. The corresponding stress history experienced by the sample is illustrated in Fig. A2 (b), where the loading and unloading process in each stress cycle is used to simulate the stress at the subsurface of a bearing inner ring when a ball rolls over. A minimum compressive pressure ( $p_{min}$ ) of 0.02 GPa was maintained throughout the test to avoid sample slipping. During the tests, the applied load, the strain measured by the gage and the position of the upper head were recorded as a function of time. In order to study the effect of maximum contact pressure ( $p_{max}$ ) on plastic strain amplitude, four  $p_{max}$  values were selected for the tests: 1.0, 1.5, 2.0 and 2.5 GPa.

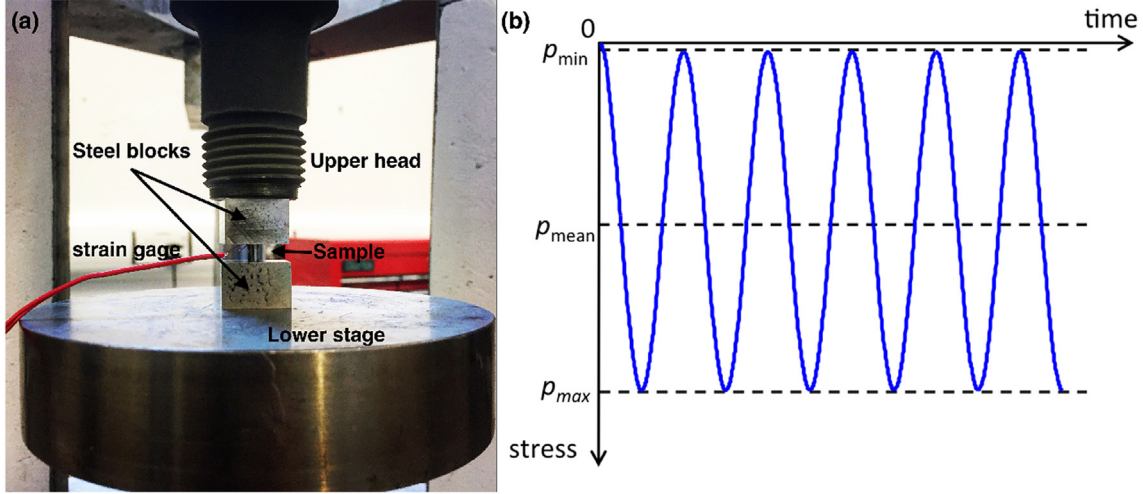


**Fig. A1.** (a) Set-up of the cyclic compression test; (b) Applied stress history of the compression test.

The results from the cyclic compression tests are presented. During the tests, the strain ( $\epsilon$ ) experienced by the sample can be directly measured by the strain gage, but due to high frequency stressing, the attachment between the strain gage and the sample surface was gradually weakened which eventually resulted in the peeling off of the strain gage. Sometimes the strain gage can peel off at the very early stage of a test, even at the first cycle. Therefore it is necessary to also calculate the strain using the position change ( $\Delta x$ ) of the upper head via  $\epsilon' = \frac{\Delta x}{l_0}$ , where  $l_0$  is the initial height of the

respectively. The loops were obtained from the sample tested at 5000 cycles under  $p_{\max} = 2.5$  GPa. For each loop, by drawing a horizontal line at the mean stress ( $p_{\text{mean}}$ ), two intersection points can be obtained, and the strain difference between these two points is the plastic normal strain amplitude ( $\Delta\epsilon$  or  $\Delta\epsilon'$ ) in this stress cycle. The determination of the plastic shear strain amplitude is also illustrated in Fig. A2.

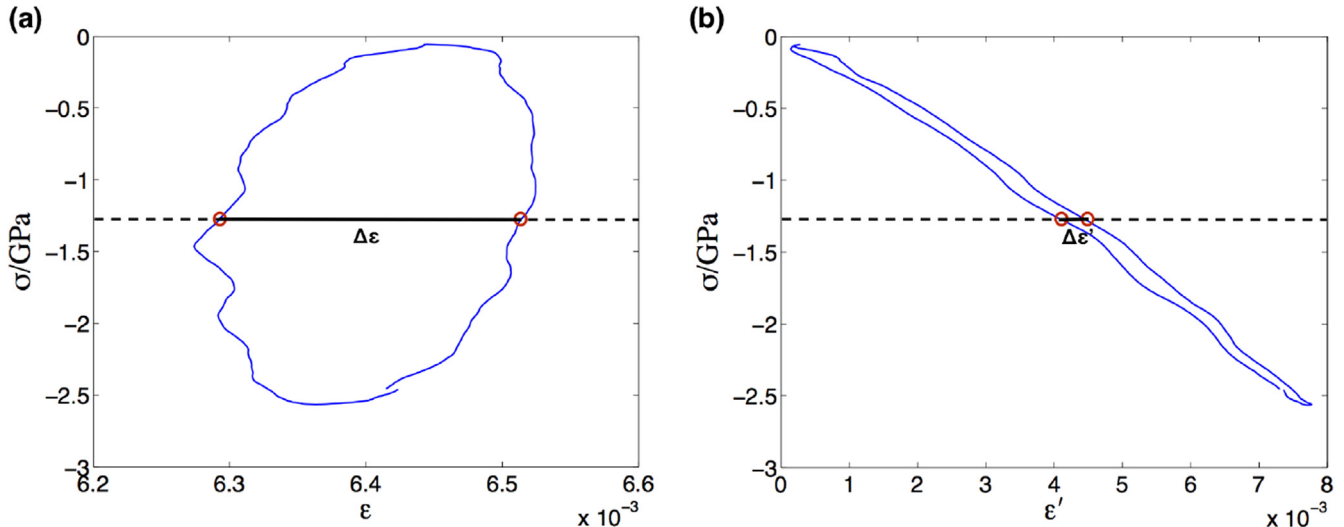


**Fig. A2.** Example of stress-strain loops of the compression test with the strain measured from the strain gage (a) and calculated from the position change of the upper head (b). The loops were taken from the sample tested at 5000 cycles under  $p_{\max} = 2.5$  GPa.

sample. However, the recorded  $\Delta x$  includes not only the deformation of the sample but also that of the two blocks holding the sample, which means the real strain ( $\epsilon$ ) of the sample is only a proportion of the strain calculated using this method. Therefore, a correction factor of 0.45, which was obtained by comparing the  $\epsilon$  values measured by the strain gages and the corresponding  $\epsilon'$  values, was introduced, i.e.,  $\epsilon = 0.45 \times \epsilon'$ . The normal stress ( $\sigma$ ) is calculated by dividing the normal load by the area of the sample.

Fig. A2 (a) and (b) show examples of the stress-strain hysteresis loops for one stress cycle with the strain measured from the strain gage and calculated from the position change of the upper head,

With increasing number of cycles, the hysteresis loops tend to become slimmer and slimmer, indicating a decrease in plastic normal strain. By collecting  $\Delta\epsilon$  and  $\Delta\epsilon_p$  values at different stages of the tests under different  $p_{\max}$  and plot them with respect to the number of cycles, the evolution of  $\Delta\epsilon$  and  $\Delta\epsilon'$  can be obtained, as shown in Fig. A3. Obvious descending trends can be seen for all four cases. Given that all the  $p_{\max}$  values are below the plastic shakedown limit and according to the classic plasticity theory, the material will eventually come to a plastic shakedown stage where the stress-strain curve follows a closed hysteresis loop with a constant plastic strain amplitude. In order to estimate this value under a

certain  $p_{\max}$ , it was postulated by Kang et al. [31] that the descending trend of  $\Delta\epsilon'$  follows the relationship:

$$\Delta\epsilon' = b_1 b_2^{\log N} + b_3 \quad (\text{A1})$$

where  $b_1, b_2$  and  $b_3$  are coefficients fitted to the experimental data. The fitted equations under different  $p_{\max}$  are shown in Fig. A3.

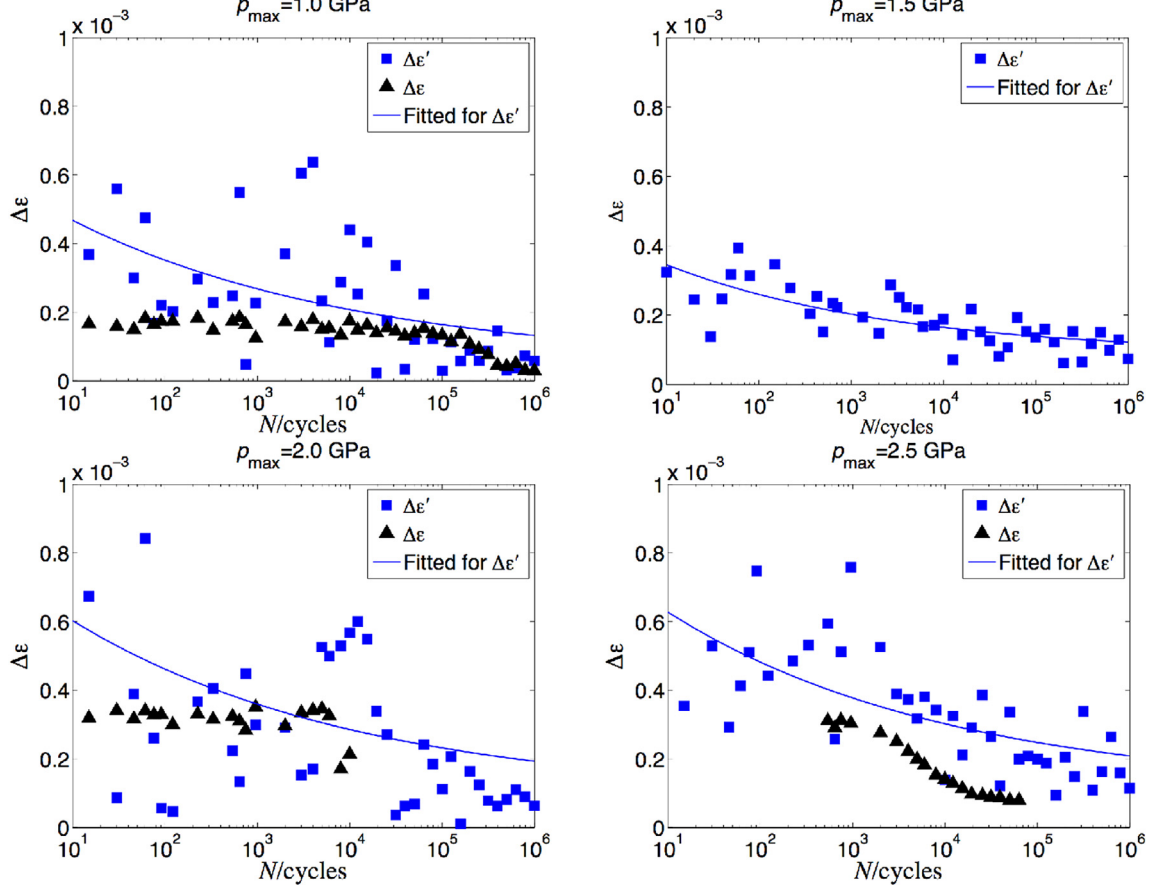


**Fig. A3.**  $\Delta\epsilon$  evolution with respect to the number of cycles under  $p_{\max} = 1.0, 1.5, 2.0$ , and  $2.5$  GPa.

Once the coefficients are determined, making  $N \rightarrow \infty$  and considering the correction factor  $0.45 \times b_3$ , it becomes the normal plastic strain amplitude at the shakedown stage. In the case of RCF, shear stress ( $\tau$ ) and shear strain ( $\gamma$ ) are more important for the formation of the microstructural alterations. According to von Mises criterion, the normal stress can be converted to equivalent shear stress via  $\tau = \sigma/\sqrt{3}$ , while the normal strain can be converted into shear strain via  $\gamma = \sqrt{3}\epsilon$ . Therefore, the plastic shear strain amplitude at the shakedown stage of fatigue, termed  $\Delta\gamma_s$ , can be obtained:

$$\Delta\gamma_s = \sqrt{3} \times 0.45 \times b_3 \quad (\text{A2})$$

Fig. A4 shows the evolution of  $\Delta\gamma_s$  with  $\tau_{\max}$ . It can be seen that  $\Delta\gamma_s$  gradually increases with increasing  $\tau$ , and a linear equation is fitted to the data for generalization:

$$\Delta\gamma_s = 4.757 \times 10^{-5} \tau_{\max} + 1.72 \times 10^{-5} \quad (\text{A3})$$

where  $\tau_{\max}$  is in GPa. In the case of RCF, the maximum shear stress ( $\tau_{\max}$ ) can be calculated from the Hertzian theory.

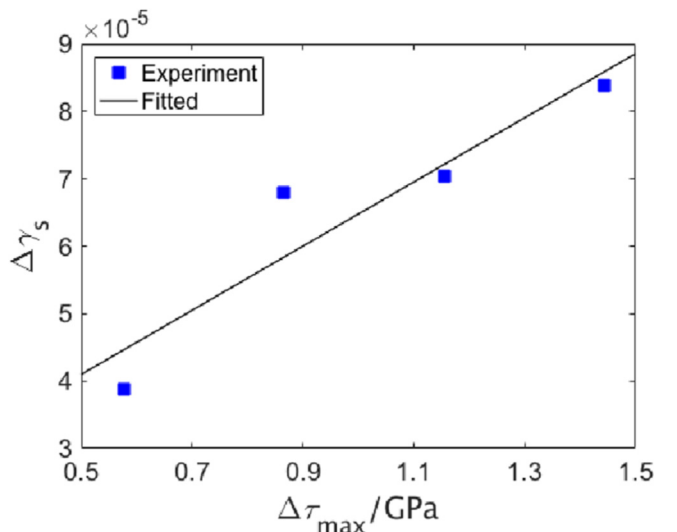


**Fig. A4.** Evolution of  $\Delta\gamma_s$  with respect to  $\tau_{\max}$ .

## References

- [1] H.K.D.H. Bhadeshia, Steels for bearings, *Prog. Mater. Sci.* 57 (2) (2012) 268–435.
- [2] J.-H. Kang, B. Hosseinkhani, P.E.J. Rivera-Díaz-del Castillo, Rolling contact fatigue in bearings: multiscale overview, *Mater. Sci. Technol.* 28 (1) (2012) 44–49.
- [3] H. Swahn, P.C. Becker, O. Vingsbo, Martensite decay during rolling contact fatigue in ball bearings, *Metall. Trans. A* 7 (8) (1976) 1099–1110.
- [4] J.A. Martin, S.F. Borgese, A.D. Eberhardt, Microstructural alterations of Rolling Bearing steel undergoing cyclic stressing, *J. Fluids Eng.* 88 (3) (1966) 555–565.
- [5] J.J. Bush, W.L. Grube, G.H. Robinson, Microstructural and residual stress changes in hardened steel due to rolling contact, *Trans. ASM* 54 (1961) 390–412.
- [6] R. Österlund, O. Vingsbo, Phase changes in fatigued ball bearings, *Metall. Trans. A* 11 (5) (1980) 701–707.
- [7] J. Buchwald, R.W. Heckel, An analysis of microstructural changes in 52100 steel bearings during cyclic stressing(microstructural changes in 52100 steel bearing inner rings during cyclic stressing, obtaining thickening rate data on white-etching regions and lenticular carbides), *ASM Trans. Q.* 61 (1968) 750–756.
- [8] N. Mitamura, H. Hidaka, S. Takaki, Microstructural development in bearing steel during rolling contact fatigue, *Mater. Sci. Forum* 539 (2007) 4255–4260.
- [9] T. Lund, Structural alterations in fatigue-tested ball-bearing steel, *Jemkonter. A* 153 (1969) 337–343.
- [10] K. Johnson, *Contact Mechanics*, Cambridge University Press, 1987.
- [11] A. P. Voskamp, Microstructural Stability and Bearing Performance, *Bearing Steel Technology*.
- [12] V. Bhargava, G.T. Hahn, C.A. Rubin, Rolling contact deformation and microstructural changes in high strength bearing steel, *Wear* 133 (1) (1989) 65–71.
- [13] I.A. Polonsky, L.M. Keer, On white etching band formation in rolling bearings, *J. Mech. Phys. Solids* 43 (4) (1995) 637–669.
- [14] T. Ochi, Y. Kusano, Change in Microstructure and Properties in the Rolling Contact Fatigue Of Bearing Steel.
- [15] A. Warhadpande, F. Sadeghi, R.D. Evans, Microstructural alterations in bearing steels under rolling contact fatigue Part 1 – historical overview, *Tribol. Trans.* 56 (3) (2013) 349–358.
- [16] A.B. Jones, Metallographic observations of ball bearing fatigue phenomena, *Proc. ASTM, Am. Soc. Test. Mater. N. Y.* 46 (1946) 1–6.
- [17] A.H. Cottrell, B.A. Bilby, Dislocation theory of yielding and strain ageing of iron, *Proc. Phys. Soc. Sect. A* 62 (1) (1949) 49.
- [18] A.P. Voskamp, Material response to rolling contact loading, *J. Tribol.* 107 (3) (1985) 359–364.
- [19] T.A. Harris, J. Skiller, R.F. Spitzer, On the fatigue life of M50 NiL rolling bearings, *Tribol. Trans.* 35 (4) (1992) 731–737.
- [20] H.-J. Christ, C. Sommer, H. Mughrabi, A.P. Voskamp, J.M. Beswick, F. Hengerer, Fatigue behaviour of three variants of the roller bearing steel sae 52100, *Fatigue & Fract. Eng. Mater. Struct.* 15 (9) (1992) 855–870.
- [21] H. Swahn, P.C. Becker, O. Vingsbo, Electron-microscope studies of carbide decay during contact fatigue in ball bearings, *Metal Sci.* 10 (1) (1976) 35–39.
- [22] M.H. Evans, White structure flaking (WSF) in wind turbine gearbox bearings: effects of butterflies and white etching cracks (WECs), *Mater. Sci. Technol.* 28 (1) (2012) 3–22.
- [23] J.L. O'Brien, A.H. King, Electron microscopy of stress-induced structural alterations near inclusions in bearing steels, *J. Basic Eng.* 88 (3) (1966) 568–571.
- [24] P. Becker, Microstructural changes around non-metallic inclusions caused by rolling-contact fatigue of ball-bearing steels, *Met. Technol.* 8 (1) (1981) 234–243.
- [25] A. Grabulov, U. Ziese, H.W. Zandbergen, TEM/SEM investigation of microstructural changes within the white etching area under rolling contact fatigue and 3-D crack reconstruction by focused ion beam, *Scr. Mater.* 57 (7) (2007) 635–638.
- [26] A. Grabulov, R. Petrov, H.W. Zandbergen, EBSD investigation of the crack initiation and TEM/FIB analyses of the microstructural changes around the cracks formed under rolling contact fatigue (RCF), *Int. J. Fatigue* 32 (3) (2010) 576–583.
- [27] Y. Murakami, H. Takemura, M. Naka, T. Ogawa, T. Momono, A. Iwamoto, S. Ishihara, Study on fatigue mechanism of bearings for automotive alternators, *NSK Tech. J.* 656 (1993) 1–14.
- [28] H. Harada, T. Mikami, M. Shibata, D. Sokai, A. Yamamoto, H. Tsubakino, Microstructural changes and crack initiation with white etching area formation under rolling/sliding contact in bearing steel, *ISIJ Int.* 45 (12) (2005) 1897–1902.
- [29] J.-H. Kang, B. Hosseinkhani, C.A. Williams, M.P. Moody, P.A.J. Bagot, P.E.J. Rivera-Díaz-del Castillo, Solute redistribution in the nanocrystalline structure formed in bearing steels, *Scr. Mater.* 69 (8) (2013) 630–633.
- [30] A.T.W. Barrow, J.-H. Kang, P.E.J. Rivera-Díaz-del Castillo, The  $\epsilon \rightarrow \eta \rightarrow \theta$  transition in 100Cr6 and its effect on mechanical properties, *Acta Mater.* 60 (6) (2012) 2805–2815.
- [31] J.-H. Kang, P.E.J. Rivera-Díaz-del Castillo, Fatigue in martensitic 100Cr6: relationship between rolling contact fatigue microstructural transitions and repetitive push testing, *Mater. Sci. Eng. A* 614 (2014) 214–222.